




## Integrated nonlinear photonics in the longwave-infrared: A roadmap

**Dingding Ren** , Department of Electrical Engineering, University of Notre Dame, Notre Dame, IN, USA; Department of Electronic Systems, Norwegian University of Science and Technology (NTNU), Trondheim, Norway

**Chao Dong, and David Burghoff**, Department of Electrical Engineering, University of Notre Dame, Notre Dame, IN, USA; Department of Electrical and Computer Engineering, University of Texas at Austin, Austin, TX, USA

Address all correspondence to Dingding Ren at [dingding.ren@ntnu.no](mailto:dingding.ren@ntnu.no)

(Received 1 May 2023; accepted 4 August 2023; published online: 22 August 2023)

### Abstract

This article presents an overview of the current status and future prospects of integrated nonlinear photonics in the long-wave infrared (LWIR) spectrum, spanning 6 to 14  $\mu\text{m}$ . This range is well-suited for applications such as chemical identification, environmental monitoring, surveillance, search and rescue, and night vision. Nevertheless, the advancement of a mature, low-loss chip-level platform for the LWIR remains in its infancy. We examine the materials growth techniques, and fabrication methods associated with integrated nonlinear photonics in the LWIR, highlighting promising platforms like chalcogenide glass, single-crystalline diamond, Ge/SiGe, and III–V compounds. Furthermore, we explore loss mechanisms, dispersion engineering, nonlinear generation of broadband supercontinuum and frequency combs, and device performance, encompassing photodetectors and modulators. Lastly, we propose a roadmap for the future development of integrated nonlinear photonics in the LWIR.

### Introduction

The longwave infrared (LWIR) region of the electromagnetic spectrum, spanning from 6 to 14  $\mu\text{m}$ , is often called the "molecular fingerprint region" due to its strong intramolecular fundamental absorption, which are orders of magnitude stronger than those in the near-infrared (NIR) and visible regions.<sup>[1]</sup> Additionally, the overlap with the second atmospheric window makes the LWIR an ideal spectral range for chemical identification and environmental monitoring. At room temperature, blackbody emission is centered at LWIR wavelengths, making LWIR photonics invaluable in applications such as surveillance, search and rescue, and night vision.<sup>[2,3]</sup>

Despite the numerous advantages of using the LWIR spectrum for advanced photonic applications, the development of a mature chip-level low-loss platform in the LWIR is still in its infancy compared to the well-developed NIR to mid-wave infrared spectrum ranges (750 nm to 5  $\mu\text{m}$ ).<sup>[4,5]</sup> Platforms such as  $\text{Si}_3\text{N}_4$  and silicon on insulator can be used to investigate nonlinear behaviors, including four-wave mixing, supercontinuum generation, ultrashort pulse formation, and entangled biphoton generation. However, these mature platforms are unsuitable for the LWIR spectrum, as most optical materials become lossy in this region. While significant advancements have been made in materials growth, fabrication processes, and powerful laser source design, further efforts are required to integrate these developments into mature platforms for integrated LWIR photonics. Nonetheless, a roadmap for research and prototyping of integrated nonlinear photonics in the LWIR is now emerging.

This review offers a comprehensive overview of the development of integrated nonlinear photonics in the LWIR region based on low-loss optical platforms. We concentrate on the

most promising and cutting-edge platforms, such as chalcogenide glass, single-crystal diamond, Ge, SiGe, and III–V compounds. We examine the methods of materials growth and intrinsic materials' loss mechanisms, along with device fabrication techniques and the critical physical and chemical properties that determine the optical performance of integrated LWIR devices. Furthermore, we will explore dispersion engineering, which enables both supercontinuum and frequency comb generations. As an example, we employ finite element simulation for dispersion engineering of a Ge microresonator, aiming for broadband frequency comb generation using a Lugiato-Lefever equation solver. These technologies have the potential to lead to innovative chip-scale sensing modalities, with implications for healthcare, environmental monitoring, and other chemical and biological sensing applications.

### LWIR materials

When selecting materials for integrated nonlinear photonics, three primary criteria must be considered: low propagation losses to be able to confine high optical fields, high nonlinear coefficients to reduce nonlinear thresholds, and good compatibility with complementary metal-oxide-semiconductor (CMOS) processes to enable accessibility for various applications.

### Optical losses

A solid's transparent window is defined by the wavelength between the high-energy side Urbach tail, which is characterized by an exponential decay of the absorption coefficient attributed to the ionization of excitons by internal electric microfields, and the vibrational bands of multiphonon

absorption on the low-energy (longer wavelength) side of the spectrum. In high-purity solid materials, multiphonon absorption processes dominate in the LWIR spectrum, limiting the selection of low-loss materials. At a given temperature, the likelihood of a multiphonon absorption process decreases with decreasing optical phonon energy. Since the atoms inside the solid material can be considered as harmonic oscillators following the lattice structure, the energy of phonon bands ( $\hbar\omega$ ) is inversely proportional to the mass of the oscillators, indicating that heavier elements have a reduced chance of undergoing a multiphonon absorption process.<sup>[6–8]</sup>

This phenomenon is particularly evident in group-IV elements. Intrinsic Si, for example, experiences optical loss larger 1 dB/cm for wavelengths longer than 7  $\mu\text{m}$  due to three-phonon absorption, and over 5 dB/cm optical loss for wavelengths longer than 10  $\mu\text{m}$  due to two-phonon absorption.<sup>[9]</sup> In contrast, Ge is located in the next period of the periodic table and exhibits onset wavelengths of three-phonon absorption at 12  $\mu\text{m}$  and two-phonon absorption at 16  $\mu\text{m}$ .<sup>[10]</sup> This demonstrates that high-purity Ge is a better choice of material for low-loss LWIR photonics compared to widely used Si photonics at shorter wavelengths.<sup>[11]</sup>

However, choosing lighter elements does not necessarily lead to higher losses in LWIR. For instance, single-crystalline diamond, composed of the lightest group-IV element (carbon), exhibits intrinsic optical loss at the 0.5 dB/cm level at 10  $\mu\text{m}$ . Although this may seem contrary to the trend observed with Si and Ge, it actually follows the trend since the multiphonon absorption is blue-shifted with lighter elements. In the case of diamond, multiphonon absorption dominates and peaks between 2.5  $\mu\text{m}$  and 6  $\mu\text{m}$ .<sup>[12]</sup> Subsequently, optical losses decrease as the operating wavelengths increase in the LWIR, making diamond a desirable material for use at wavelengths longer than 10  $\mu\text{m}$  in LWIR.

In addition to using crystalline materials like diamond and Ge for low-loss LWIR platforms, amorphous materials with heavier elements, such as chalcogenide glasses, are also suitable for this purpose and can cover most of the LWIR spectrum. The absorption characteristics of these chalcogenide glasses within the transparent window are greatly influenced by various factors such as local disorders, defects, impurities, free carrier density, and lattice vibrations. However, the multiphonon absorption of these glasses sets the low-loss cut-off wavelength for high-purity, high-resistance chalcogenide glasses on the low-energy side of the transparent window.<sup>[13]</sup>

In summary, it is crucial to develop innovative methods for material growth and improve fabrication processes in order to minimize impairments and reach the absorption limit determined by the multiphonon process. This maximizes the use of low-loss materials, whose performance is summarized in Fig. 1, for integrated nonlinear photonics in the LWIR. As

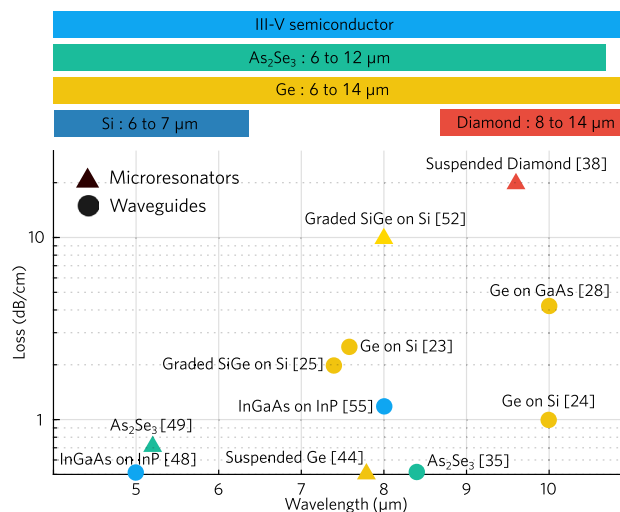


**Figure 1.** The LWIR transparency windows (where material attenuation is  $< 1$  dB/cm) of III-V semiconductor,  $\text{As}_2\text{Se}_3$ , Ge/SiGe, Si, and diamond. The triangles and disks represented the performance of chip-scale devices of microresonators and waveguides, respectively.

the field progresses, continued research and development in material engineering will play a significant role in expanding the potential applications of LWIR photonics, opening new possibilities in healthcare, environmental monitoring, and other chemical and biological sensing applications.

## Nonlinearity

For pulse formation or frequency conversion, nonlinear effects benefit from a larger refractive index, which results in higher material susceptibility and lower thresholds for these optical processes when properly phase-matched. The  $\chi^{(3)}$  susceptibility of Ge is estimated to be an order of magnitude higher than that in Si.<sup>[14]</sup> This leads to a very large Kerr nonlinearity  $n_2$  of Ge on the order of  $2 \times 10^{-17} \text{ m}^2/\text{W}$ , which is an order of magnitude higher than chalcogenide glass and Si. It is important to note that the two-photon absorption (TPA) in Ge peaks at about 3  $\mu\text{m}$ , chalcogenide glass and Si peak at about 2  $\mu\text{m}$  and diamond at about 450 nm. These TPA features are far from the LWIR wavelengths, meaning that the nonlinear coefficients in these materials are flattened throughout the entire LWIR spectrum. We estimate the nonlinear coefficients for chalcogenide glass and diamond at LWIR in the order of  $10^{-18} \text{ m}^2/\text{W}$  and  $10^{-20} \text{ m}^2/\text{W}$ , respectively, based on the measurements at shorter wavelength.<sup>[15,16]</sup> The  $n_2$  value of SiGe alloy should be between the values of Ge and Si, i.e.,  $10^{-17} \text{ m}^2/\text{W}$  and  $10^{-18} \text{ m}^2/\text{W}$ . The nonlinearity of III-V materials, specifically InGaAs and GaAsSb, has recently been measured using waveguide geometry to be  $5 \times 10^{-17} \text{ m}^2/\text{W}$  and  $8.5 \times 10^{-17} \text{ m}^2/\text{W}$ , respectively. These materials exhibit enhanced nonlinearity due to the incorporation of heavy elements in their composition.<sup>[17]</sup>

## Fabrication methods and device performance

The choice of materials for integrated applications in the LWIR is limited not only by multiphonon bands but also by the requirement of compatibility with CMOS technology, which excludes a significant number of low-loss materials such as fluorides and bromides. In this section, we will primarily revolve around Ge, SiGe, diamond, and chalcogenide glass, which are compatible with the industry-dominant silicon technology.

### Epitaxial growth of Ge-based materials

Although Ge is an excellent choice of material for LWIR with low intrinsic optical loss and giant nonlinear coefficients, the development of LWIR integrated photonics, including integrated nonlinear photonics using Ge as the effective optical medium, has been slow until high-quality epitaxy growth becomes available. Pure Si and Ge have lattice constants of 5.4310 Å and 5.6575 Å, respectively. The difference in lattice constants results in a 4.2% lattice mismatch, which makes the direct epitaxy growth of Ge on Si challenging.<sup>[18]</sup> Two-temperature growth schemes have been adopted: a low-temperature nucleation step reduces the threading dislocation density between the Ge active material and the Si substrate due to the large lattice mismatch, and a high-temperature epitaxy growth step ensures the grown bulk material's good optical quality.<sup>[19,20]</sup> A combination of defect-selective wet etching and scanning electron microscopy (SEM) was used to characterize the threading dislocation density of a 3 μm Ge epitaxial layer on a Si wafer grown via a reduced pressure chemical vapor deposition. It was estimated that the threading dislocation density was around  $2 \times 10^7$  to  $5 \times 10^7$  cm<sup>-2</sup>.<sup>[21]</sup>

A Ge-on-Si photonic “cut-back” circuit for waveguide propagation loss measurement has been fabricated with grating coupler for fully integrated LWIR photonics.<sup>[22,23]</sup> Over the spectral range 7.5–8.5 μm, the measured waveguide loss increases from 3.0 dB/cm to nearly 20 dB/cm with a minimum of 2.5 dB/cm at 7.575 μm, marked as a yellow disk in Fig. 1. In a similar study, researchers used a ZnSe lens to directly couple the LWIR laser from a quantum cascade laser (QCL) in free space to the waveguide.<sup>[24]</sup> The optical loss was estimated by thermally tuning the refractive index of the Ge-on-Si waveguide, which modulated the transmitted signal based on a simple theory of the Fabry-Perot cavity. The optical loss as low as ~1 dB/cm for ≥10 μm wavelengths has been reported for the TE polarization, marked as a yellow disk on the longer wavelength side in Fig. 1. Surprisingly, they found a decrease in optical loss from Ge with increasing wavelength from 7.5 to 11 μm, presenting a promising perspective for extending the operation wavelength further into the red-side of the LWIR spectrum.

Instead of directly growing Ge on top of Si substrate, an epitaxially grown graded SiGe buffer can both mitigate the lattice mismatch and push the optical mode away from the relatively lossy Si substrate. For application in the blue-side of the LWIR

spectrum, a developed SiGe/Si stack has been used to fabricate straight waveguides, which presented losses as low as 2 dB/cm at 7.4 μm,<sup>[25]</sup> marked as yellow disk in Fig. 1. To push the working wavelength longer with lower losses, a high-Ge composition SiGe waveguide is preferred. The Ge-rich SiGe waveguide on Si can efficiently guide light from 5 to 11 μm. By tuning the laser wavelength from 5.1 to 8 μm, the optical losses increased from 0.5 to 1.2 dB/cm. Pushing the wavelength longer from 9.5 to 11.2 μm, the optical losses stayed below 3 dB/cm.<sup>[26]</sup>

Other than using a highly lattice-mismatched Si substrate, growing on a lattice-matched substrate, e.g., GaAs, can significantly reduce the defect density that maintains the optical loss as low as the bulk Ge. The multiphonon absorption in intrinsic GaAs is below 0.05 dB/cm until 11 μm and about 2 dB/cm at 14 μm, presenting an appealing alternative to Si substrate for LWIR photonics.<sup>[27]</sup> However, the ridge-waveguide device of Ge made from the epitaxy process shows an optical loss of approximately 4.2 dB/cm at 10 μm wavelength, marked as a yellow disk in Fig. 1, which is almost 100 times larger than the theoretical value.<sup>[28]</sup> This could come from unintentional doping characteristics of the epitaxial layer of Ge on GaAs films.<sup>[29]</sup> During Ge epitaxy, the volatile As-species (e.g., As<sub>2</sub> and As<sub>4</sub>) in the background of the growth chamber will be incorporated via gas phase transport, leading to the unintentional n-type doping in the Ge epitaxial layer. In addition, Ga atoms can also be incorporated at the interface with the Ge layer through a surface exchange process at the elevated temperature during growth, resulting in a layer of Ga-rich interface with potentially increased optical loss at LWIR. Compared to the growth on Si substrate, epitaxial growth of Ge on GaAs have solved the lattice mismatch issue and showed improved optical properties, while practically it introduces other challenges that should be addressed to reach the limit of Ge on the GaAs platform.

### Growth of chalcogenide glass and diamond

Thanks to the amorphous nature of chalcogenide glass with low phonon energies, thin film formation can be achieved by vaporizing high-purity bulk materials using ultra-fast pulsed laser deposition,<sup>[30]</sup> RF magnetron sputtering,<sup>[31]</sup> and thermal evaporation.<sup>[32]</sup> For nonlinear photonic applications, chalcogenide glass with a high glass transition temperature is preferred due to its slower structural relaxation resulting from stronger chemical bonds.<sup>[33]</sup> Typical low-loss chalcogenide glasses include As<sub>2</sub>Se<sub>3</sub>, As<sub>2</sub>S<sub>3</sub>, and Ge<sub>23</sub>Sb<sub>7</sub>S<sub>70</sub>.<sup>[34]</sup> An As<sub>2</sub>Se<sub>3</sub> and As<sub>2</sub>S<sub>3</sub> bilayer were deposited on top of SiO<sub>2</sub>, with waveguides fabricated using As<sub>2</sub>S<sub>3</sub> as the bottom cladding and the optical mode confined in the high-refractive-index As<sub>2</sub>Se<sub>3</sub> layer.<sup>[35]</sup> At 8.4 μm, optical losses as low as 0.5 dB/cm, marked as a green disk in Fig. 1, were measured using a QCL with TE polarization end-fire coupled into the waveguides. However, the metastable nature of chalcogenide glass results in non-negligible drifts in their optical properties, such as changes in refractive index over

time, which is an unavoidable issue to be resolved for a robust photonic platform at LWIR, particularly for on-chip nonlinear photonics with very high power continuous wave excitation.<sup>[36]</sup>

In contrast to amorphous glass, single-crystalline diamond favors homoepitaxy growth with high crystal quality. Microwave plasma chemical vapor deposition is one of the most popular growth techniques. Using a patterned diamond membrane as the homoepitaxy substrate, the overgrown single-crystalline diamond exhibited significantly enhanced optical properties, such as strong luminescence, narrow Raman peaks, and the appearance of NV center spin lifetimes, which are characteristic of high-quality bulk diamond.<sup>[37]</sup> By using the patterned diamond membrane as the growth substrate, the diamond template can be entirely etch-removed, leaving the highest quality overgrown diamond material for photonic device applications in the LWIR. However, only a few studies have reported the optical losses of integrated photonic devices at LWIR, with optical losses of around 20 dB/cm marked as a red triangle in Fig. 1.<sup>[38]</sup>

### Device design and fabrication method

CMOS process compatibility is essential for foundry-level production to reduce process costs and facilitate technology commercialization. These processes include lithography, metal and oxide deposition, and plasma dry etching. Fortunately, Ge shares the same etching chemistry as Si.  $\text{SF}_6$  chemistry is often used to dry etch the Ge active layer, with  $\text{C}_4\text{F}_8$  as the sidewall passivation agent.<sup>[39]</sup> High-aspect-ratio Ge waveguides with smooth sidewalls have been etched using the  $\text{SF}_6$  and  $\text{C}_4\text{F}_8$  chemistry, with masks defined by electron beam lithography.<sup>[23,24]</sup> The epitaxial Ge layer was partially etched, and the optical mode was confined in the Ge part, forming rib waveguides. Since the  $\text{SF}_6$  and  $\text{C}_4\text{F}_8$  chemistry works for both Ge and Si, it is not surprising that these dry etching processes also work for SiGe alloy.

Instead of acting as a passivation agent, the fabrication of chalcogenide glass waveguides relies on  $\text{CF}_4$  chemistry for dry etching processes.<sup>[30]</sup> Plasma etching using a  $\text{CF}_4/\text{O}_2$  gas mixture showed a significant increase in etching rate compared to that using  $\text{CF}_4$  gas alone for chalcogenide films. To increase the aspect ratio of the waveguide, it is necessary to increase the substrate bias as the content of heavy Se atoms in Se-based glasses increases. In addition to the dry etching process, a lift-off process has been developed for both ridge and rib chalcogenide glass waveguides.<sup>[40]</sup> The rib waveguides have reduced optical loss, suggesting that sidewall roughness is one of the predominant loss mechanisms.

For the fabrication of diamond waveguides and microresonators, oxygen plasma can be used to thin down the single-crystalline diamond bulk material to the targeted thickness. For NIR applications, diamond is directly integrated onto  $\text{SiO}_2/\text{Si}$  substrates, with the bottom  $\text{SiO}_2$  layer serving as the cladding layer. However,  $\text{SiO}_2$  becomes lossy at LWIR wavelengths, making air cladding more suitable for integrated LWIR devices. To create suspended diamond structures, anisotropic oxygen-based plasma etching can be performed at an oblique angle

to the substrate surface.<sup>[41]</sup> This technique will be discussed in detail for suspended structure. We note that, due to the low etching rate of diamond using oxygen plasma, using a hard mask, such as  $\text{Si}_3\text{N}_4$ , is preferred.<sup>[42,43]</sup> Further device manufacturing methods should be explored to close the gap between actual device performance and theoretical loss estimates from the literature.

Due to the limited choice of low-loss materials at LWIR, suspending the waveguiding part of the microresonator and using air cladding can, in principle, approach the intrinsic transparency limit of the materials due to multiphonon absorption. Figure 2(a) shows a schematic of the detailed fabrication process of a non-epitaxial Ge microresonator made from a high-resistivity native Ge wafer, and the process consists of the wafer bonding process, electron beam lithography, dry etching, surface polishing processes, and resonator suspension using hydrofluoric acid.<sup>[44]</sup> The described fabrication processes and device designs offer potential solutions for achieving low-loss and high-performance integrated LWIR photonic devices. It is crucial to continue optimizing the material integration, etching, and device design to improve the performance of integrated LWIR devices. The new integration method and device design will unleash the true potential of high-quality materials with low intrinsic losses, such as Ge, chalcogenide glasses, and diamond.

In addition to the suspension process utilizing the heterointerface between different materials, suspended microresonators can also be fabricated within a homogeneous medium by carefully designing the dry etching conditions, such as sidewall passivation and isotropic plasma.<sup>[43]</sup> The quasi-isotropic etching uses an unbiased oxygen plasma for crystal plane selective etching. It generates undercuts similar to the SCREAM process in silicon.<sup>[45]</sup> The schematic of the fabrication of suspended diamond whispering-gallery-mode (WGM) microresonators is shown in Fig. 2(b), with SEM images of magnified individual resonators and an array of microresonators in Fig. 2(c) and (d), respectively. In contrast to the fabrication process of both suspended microresonators, there is no need for substrate thinning, and the microresonators can be devised within bulk materials. However, the performance of the suspended structure made inside the bulk materials strongly depends on the smoothness of the bottom facet of the microresonator, which is formed by isotropic etching. This is different from the suspended Ge microresonator, where the bottom surface has a polishing finish from the as-received wafer, as shown in Fig. 2(b).

Aside from suspended WGM microresonators, waveguides can also be suspended utilizing a semiconductor on insulator technology. Figure 2(e) shows the fabrication of a suspended Ge waveguide, which begins with the epitaxial growth of a Ge layer on a Si-on-insulator wafer. Then, the dimensions of a rib waveguide were defined by e-beam lithography and dry etching. To suspend the defined Ge waveguide, an array of holes was created alongside the waveguide, providing an open channel to chemically remove the buried oxide (BOX) layer using a wet etchant. In addition, these arrays of holes provide



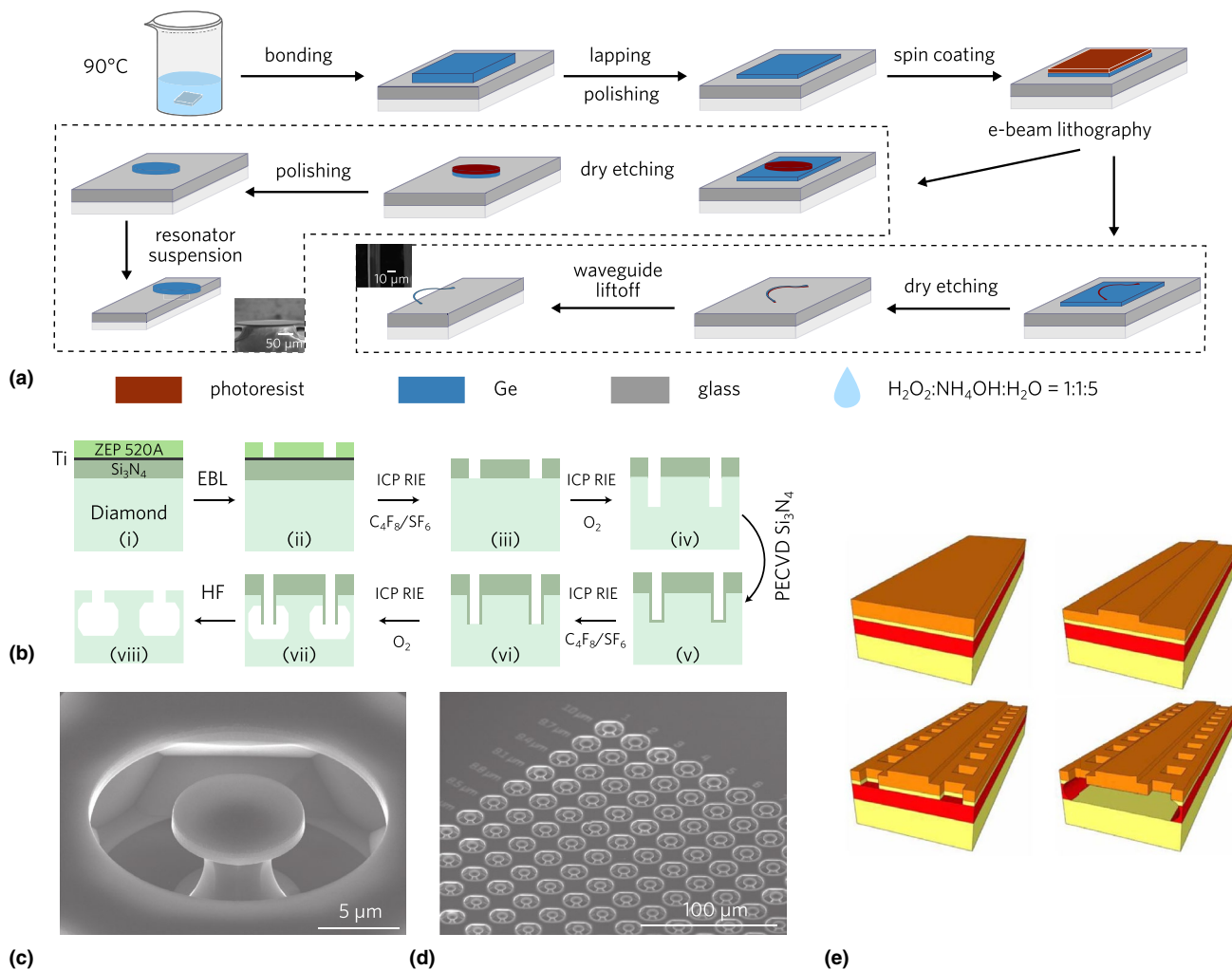


**Figure 2.** (a) Overview of the fabrication procedure of a native Ge microresonator with a 450 μm diameter disk supported by a glass pillar, adapted from Ref. 44 with permission. (b) Schematic of the suspended diamond microdisk fabrication inside a diamond substrate. (c) A 45° rotated SEM image of a 7.9 μm diameter diamond microdisk in a diamond chip. (d) Overview of an array of fabricated diamond microdisks, reused from Ref. 43 with permission. (e) Fabrication process flow of the suspended Ge waveguides from the initial Ge-on-SOI wafer to waveguide definition using e-beam lithography and etching, hole patterning and exposure of the BOX, and wet etching using HF and TMAH, adapted with permission from Ref. 47 © The Optical Society.

mechanical support for the waveguide and enhance the confinement of optical modes due to the air cladding. The sample is also immersed in a 25% aqueous solution of anisotropic tetramethylammonium hydroxide (TMAH) at room temperature. It completely removes the Si layer from the top of the silicon-on-insulator wafer, as well as part of the Si substrate, further increasing the air gap below the waveguide. We note that a previous study of a similar structure of Si suspended waveguide reports an optical loss of 3.1 dB/cm at 7.67 μm, approaching the limit set by the multiphonon absorption of Si.<sup>[46]</sup> However, the suspended Ge waveguide only reached 2.6 dB/cm, which is not close to the limit set by the multiphonon process.<sup>[47]</sup> This could be due to defects generated from the epitaxial growth of the Ge layer on the highly mismatched Si substrate. These defects can become midgap recombination

centers and deteriorate the optical transparency of the suspended Ge waveguide.

Not only is the fabrication of high-performance LWIR waveguides a challenging endeavor, but it also presents significant difficulties in measuring the devices because the LWIR signal is hard to visualize, and there is considerable background thermal noise due to blackbody radiation. Curved waveguides have been made to minimize scattering signals.<sup>[44,48]</sup> This is crucial because the lock-in amplifier used will maximize the signal, part of which could come from other paths of light than the waveguide in the LWIR. Instead of using waveguides, measuring the linewidth of resonance from a microresonator is another alternative and robust method for evaluating the performance of intrinsic LWIR materials. High-index-contrast As<sub>2</sub>Se<sub>3</sub> chalcogenide glass has been waveguide-coupled to an

As<sub>2</sub>Se<sub>3</sub> microresonator monolithically integrated on silicon, fabricated using optical lithography and a lift-off process.<sup>[49]</sup> Although it exhibited a high intrinsic quality factor of  $2 \times 10^5$  at 5.2  $\mu\text{m}$  wavelength, marked as a green triangle in Fig. 1, the operating wavelength did not reach the LWIR spectrum, and there is no report of a successful LWIR As<sub>2</sub>Se<sub>3</sub> microresonator yet.<sup>[50]</sup> As for other fully integrated planar microresonators, devices fabricated from epitaxially grown Ge<sup>[51]</sup> and SiGe,<sup>[52]</sup> marked as a yellow triangle in Fig. 1, have only shown a quality ( $Q$ ) factor of several thousand in the LWIR. In comparison to the suspended high-quality Ge microresonator with a  $Q$  factor of  $2.5 \times 10^5$  at 7.8  $\mu\text{m}$ ,<sup>[44]</sup> marked as a yellow triangle in Fig. 1, this strongly suggests that a new strategy is needed to mitigate material degradation in realizing fully integrated LWIR photonics.

### Integrated III–V platforms

To develop fully integrated LWIR photonics, one major challenge to consider is the integration of passive optical components with laser sources. A promising solution for this is the monolithic combination of III–V photonic platforms with III–V solid-state lasers, such as QCLs, through epitaxy.<sup>[53]</sup> Two potential candidates for low-loss passive components are In<sub>0.53</sub>Ga<sub>0.47</sub>As and GaAs<sub>0.51</sub>Sb<sub>0.49</sub>, as these ternaries are lattice-matched to the InP substrate. As a demonstration, a QCL and an In<sub>0.53</sub>Ga<sub>0.47</sub>As waveguide have been grown bottom-up on a single chip. Using a tapered adiabatic coupler, the emission from the QCL has been successfully coupled into the In<sub>0.53</sub>Ga<sub>0.47</sub>As waveguide, which are vertically separated by cladding layers.<sup>[54]</sup>

While multiphonon absorption is not the limiting factor for pushing the operating wavelength further into the LWIR range, integrated III–V photonic devices may suffer from free-carrier absorption resulting from the non-ideal epitaxy growth process, as briefly discussed in session "Epitaxial growth of Ge-based materials" using Ge on GaAs as an example. To achieve the low-loss limit set by multiphonon absorption for III–V integrated photonics, it will be crucial to reduce the incorporation of background impurities and minimize defect formation. Recently, buried InGaAs/InP waveguide shows optical loss as low as 1.2 dB/cm at 8  $\mu\text{m}$  with direct butt coupling to QCL, marked as a blue disk in Fig. 1, enabling the frequency comb generation in the LWIR.<sup>[55]</sup> In addition, both high-quality waveguides and microresonators have been demonstrated at 5  $\mu\text{m}$ , with an optical loss as low as 0.5 dB/cm, marked as a blue disk in Fig. 1.<sup>[48]</sup> By utilizing two single-mode QCL lasers, a sideband generated at 4.98  $\mu\text{m}$  has been observed through a four-wave mixing process.<sup>[17]</sup>

### Nonlinear photonics Laser sources

To accurately measure the performance of integrated LWIR photonic devices, such as waveguide optical losses, a single-wavelength LWIR laser with wide tunability is essential.

Solid-state QCLs are the most suitable light source for this purpose as they provide coherent single-wavelength optical emission covering the entire LWIR spectrum range.<sup>[56–58]</sup> In particular, QCLs using an InGaAs/AlInAs/InP material system can generate multi-watt level output power with more than 20% wall-plug efficiency at room temperature from 6 to 14  $\mu\text{m}$ .<sup>[59,60]</sup>

Distributed feedback (DFB) QCLs can provide narrow single-wavelength emission in the LWIR by integrating a grating over the waveguiding structure using a top-down etching process.<sup>[61]</sup> The wavelength of DFB-QCL emission can be tuned by changing the temperature and the injection current of the laser. The change of temperature tunes the refractive index of the cavity, and the change of injection current modifies the gain curvature. By fine-tuning both the injection current and DFB-QCL temperature, a mode-hop free continuous scan can be realized over  $5 \text{ cm}^{-1}$  to measure the linewidth of the cavity below 100 MHz in the LWIR.<sup>[44]</sup> However, the thermal tuning speed is limited by the laser's thermal management.

To achieve broader and faster wavelength tunability for QCL, an external cavity (EC) with grating can be coupled to the QCL by feedback. Using a broad bound-to-continuum design of gain structure, the grating-coupled EC-QCL can be tuned over  $150 \text{ cm}^{-1}$  at 10  $\mu\text{m}$ .<sup>[62]</sup> This broad tuning range is particularly useful for characterizing the dispersion of integrated devices.<sup>[63]</sup> However, mode hopping and inaccurate control of laser wavelength due to the change of grating position are major challenges for measuring high-quality optical devices using EC-QCL at LWIR. This is because it is technically challenging to precisely place the gratings at the sweet spot, and the change of mirror position results in a shift of the exact lasing wavelength.

To enable specific applications such as supercontinuum generation, ultrafast pulsed laser sources with high-peak intensity are required to trigger spectral broadening effects like soliton fission.<sup>[64]</sup> This typically necessitates ultrashort pulses with an average power at the watt level from major laser sources such as optical parametric amplifiers (OPAs). There have been few reports of OPAs that can be integrated at the chip level, let alone in the LWIR spectrum.<sup>[65]</sup> However, with the rapid development of low-loss LWIR photonic platforms, as described in this prospective, it is hoped that all laser sources for pumping LWIR nonlinear photonics can eventually be integrated onto a single chip.

One of the most promising solutions to integrate III–V laser sources on a CMOS platform is the direct growth of the laser structure on Si. InAs/AlSb QCLs have been grown on Si substrates with a 6° miscut toward the [110] direction using molecular beam epitaxy, exhibiting room temperature emission at 11  $\mu\text{m}$ .<sup>[53]</sup> This direct growth of III–V QCL lasers on Si is also compatible with the InP platform through the growth of a GaAs and InP superlattice buffer.<sup>[66]</sup> With its capability for room-temperature operation in the LWIR range on Si substrates, this approach establishes a connection between integrated III–V photonics and CMOS platforms, as demonstrated by the full integration of lasers and passive waveguides discussed in

section "Integrated III-V platforms".<sup>[54]</sup> Other solutions, such as transfer printing,<sup>[67]</sup> can also be useful for integrating LWIR laser sources into a passive component chip.

In addition to the advantage of miniaturization, optical feedback from passive microresonators can narrow the linewidth of the integrated laser and extend the wavelength tuning range by locally heating the microresonator. This technique has been well-established in the NIR telecom band but remains largely unexplored in the LWIR spectrum.<sup>[68]</sup>

### Dispersion engineering

In on-chip nonlinear photonics, optical modes are confined using cladding materials. By controlling the optical confinement, it is possible to fine-tune the effective refractive index, the free spectral range (FSR), and the group velocity dispersion. This is crucial for nonlinear engineering, as the Kerr effect induces a material's dispersion  $\chi^{(3)}$  term that causes a phase delay due to the high optical intensity in a medium. To compensate for this nonlinear change in the refractive index, the group velocity dispersion must be adjusted to the anomalous regime to keep the cavity modes at equal spacing. This is essential for parametric spectrum broadening and frequency comb generation.<sup>[69]</sup>

We begin our analysis by calculating the resonant frequencies that can occur within an integrated LWIR photonic cavity, as described in our recent study.<sup>[44]</sup> As an example, we

can consider a WGM microresonator and calculate one of its eigenmodes at a wavelength of 7.8  $\mu\text{m}$  using finite element simulation. The confined optical mode is depicted in Fig. 3(a). To investigate the change in resonant frequency inside the microcavity for LWIR nonlinear optics, we sweep the wavelength in the LWIR range from 6 to 14  $\mu\text{m}$  and plot the free spectral range (FSR) (i.e.,  $D_1$ ) and the change in FSR per mode ( $D_2$ ) in Fig. 3(b) and (c), respectively. We can express the resonant frequency of the  $\mu$ th mode in terms of nonlinear optical parameters, as follows:

$$\omega_\mu = \omega_0 + D_1\mu + \frac{1}{2}D_2\mu^2 + \dots \quad (1)$$

where  $\mu$  is the mode number and  $\omega_\mu$  is the  $\mu$ th frequency.<sup>[70]</sup> When the thickness of the microresonator is large (e.g., 12.5  $\mu\text{m}$ ), the increase in eigenmode wavelength results in an increase in FSR, suggesting normal dispersion [negative  $D_2$  in Fig. 3(c)]. However, when the thickness is reduced, the increase in eigenmode wavelength leads to anomalous dispersion [positive  $D_2$  in Fig. 3(c)], which can be understood as the increase in confinement dominating the cavity dispersion.

In addition to the WGM microresonator, which confines the optical mode at the edge of the cavity, an optical waveguide can confine the optical mode tightly with cladding layers in all four directions. By controlling the dimension of the waveguide, it is possible to precisely control the cavity

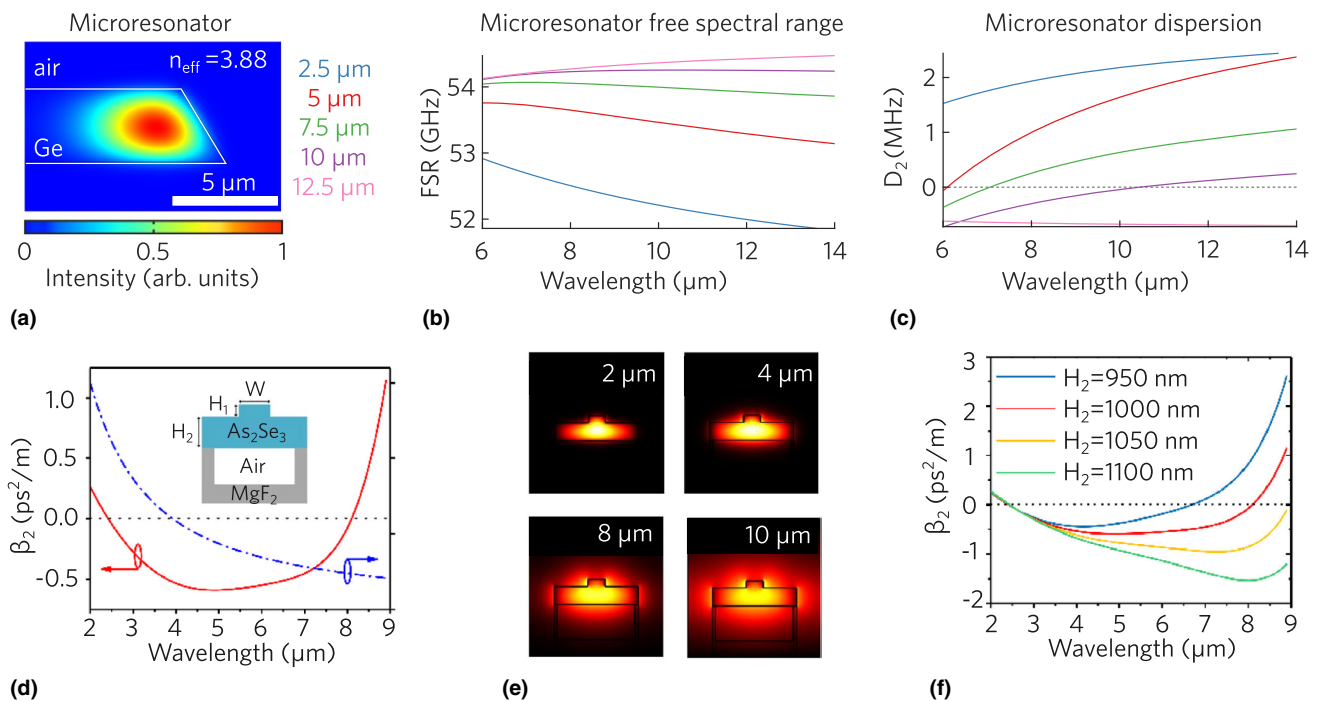


**Figure 3.** (a) FEM simulation of the guided quasi-TE mode in the Ge WGM microresonator from Fig. 1(a), (b), (c) Calculated FSR and dispersion ( $D_2$ ) versus waveguide thickness from a Adpated with permission from Ref. 44 (d) Calculated GVD and nonlinear coefficient as functions of wavelength from the suspended  $\text{As}_2\text{Se}_3$  ridge waveguide shown in the inset. (e) The mode field distributions of the quasi-TE mode calculated at wavelengths 2, 4, 8, and 10  $\mu\text{m}$ . (f) The GVD coefficients of the quasi-TE mode as functions of wavelength when  $H_2$  (as shown in the inset of d.) is varied. Adapted with permission from Ref. 71 © The Optical Society.

dispersion over a wide range. Figure 3(d) depicts a schematic of a suspended  $\text{As}_2\text{Se}_3$  rib waveguide on an  $\text{MgF}_2$  substrate.<sup>[71]</sup> The full-vector finite element method was utilized to simulate the dispersion characteristics of the waveguide with different geometrical parameters, such as  $H_1$ ,  $H_2$ , and  $W$  shown in the inset of Fig. 3(d). Using finite element method simulation with geometry  $H_1=1\ \mu\text{m}$ ,  $H_2=0.4\ \mu\text{m}$ , and  $W=1\ \mu\text{m}$ , the optical quasi-TE mode at  $2\ \mu\text{m}$ ,  $4\ \mu\text{m}$ ,  $8\ \mu\text{m}$ , and  $10\ \mu\text{m}$  is shown in Fig. 3(e). In Fig. 3(f), the second-order dispersion  $\beta_2$  and the nonlinear coefficient  $\gamma$  are plotted from  $2$  to  $9\ \mu\text{m}$ , with anomalous group velocity dispersion from  $2.5$  to  $8\ \mu\text{m}$ , which is suitable for broadband supercontinuum generation based on soliton fission. To extend the anomalous group velocity dispersion ( $\beta_2 < 0$ ) toward longer wavelengths into the LWIR, the geometry of the rib waveguide can be engineered. As the height  $H_2$  increases from  $950$  to  $1050\ \text{nm}$ , the zero dispersion point extends from  $7$  to  $9\ \mu\text{m}$  in Fig. 3(f). This can be beneficial for broader band nonlinear processes, such as supercontinuum and frequency comb generation.

### Supercontinuum generation

A supercontinuum source in the LWIR can emit an ultra-broadband spectrum of light covering the entire LWIR spectral range. The supercontinuum emission is generated by passing a high-intensity laser pulse, typically with fs-level duration, from an OPA through a waveguide. The strong nonlinearity inside the waveguide coherently broadens the spectrum, which can cover a wide range of spectrum from  $6$  to  $14\ \mu\text{m}$ . Due to the strong interaction with molecules, an LWIR supercontinuum emission can be used for various applications, such as gas detection, chemical analysis, and remote sensing by identifying multiple chemicals simultaneously.

The basic supercontinuum generation process can be simulated using the generalized nonlinear Schrödinger equation (GNLSE) as follows:

$$\frac{\partial A}{\partial z} = -\frac{\alpha}{2} + i \sum_{k>2} \frac{\beta_k}{k!} \left( i \frac{\partial}{\partial t} \right)^k E + i\gamma \left( 1 + i\tau_{shock} \frac{\partial}{\partial t} \right) |A|^2 A, \quad (2)$$

where  $A$  is the temporal envelope of the pulse,  $z$  is the distance along the propagation direction,  $\alpha$  is the linear propagation loss coefficient,  $\beta_k$  is the  $k$ th order of dispersion,  $t$  is the time in the comoving frame at the phase velocity of the envelope, and  $\tau_{shock}$  is a time scale describing the self-steepening effect and first-order frequency dependence of the modal area.<sup>[72,73]</sup> Although the GNLSE can simulate supercontinuum generation with a variety of dispersion engineering strategies, including anomalous GVD,<sup>[64,74]</sup> all normal GVD,<sup>[75]</sup> and low and flat dispersion curves that multiply cross the zero dispersion curve<sup>[76]</sup> at LWIR, the nonlinear terms should be adjusted according to the existing nonlinear phenomena inside the cavity.

With the rich history of supercontinuum research in fiber optics and the availability of powerful pump sources in the

LWIR, supercontinuum generation from chip-integrated waveguides has been able to cover the LWIR spectrum with the fast development of low-loss LWIR materials and device processing. Recently, Ge-rich SiGe waveguides with graded SiGe buffer have been shown to offer SC generation from  $3$  to  $13\ \mu\text{m}$  with anomalous dispersion.<sup>[64]</sup> By utilizing soliton fission processes on high-power, fs-short input pulses, the high-order soliton can be broken up into its constituent fundamental solitons, which simultaneously broaden the output spectrum.<sup>[64,77]</sup> In addition, two dispersive waves at zero crossing of the group velocity dispersion shown in Fig. 4(a) can push the supercontinuum spectrum broader, leading to state-of-the-art bandwidth of two-octave spanning supercontinuum generation with a  $-30\ \text{dB}$  criterion in Fig. 4(d). Efforts have also been made to engineer the dispersion of the waveguide to have a low and flat dispersion curve that crosses the zero dispersion curve multiple times in Fig. 4(c), leading to full coverage of supercontinuum generation from  $6$  to  $14\ \mu\text{m}$  in Fig. 4(f) using suspended Ge-on-Si waveguides.<sup>[76]</sup>

In addition to supercontinuum generation in the anomalous dispersion regime, waveguides in the all-normal dispersion regime, as shown in Fig. 4(b), can also generate octave-spanning supercontinuum spectra approaching the LWIR. The mechanisms behind this phenomenon are likely self-phase modulation ( $\tau_{shock}$  term in GNLSE equation 2), optical wave breaking, and stimulated Raman scattering.<sup>[75,78,79]</sup> Supercontinuum generation in the normal dispersion regime, as shown in Fig. 4(e), can maintain a correlated phase relationship with the seeding laser. Compared to supercontinuum spectra generated from soliton fission processes, which may experience pulse splitting with complicated phase noise and intensity fluctuation, supercontinuum spectra generated in the normal dispersion regime are promising to be more coherent with flat supercontinuum spectra, making them suitable for high-resolution and high-coherence applications.<sup>[80]</sup>

In addition to the Ge and SiGe systems, chalcogenide waveguides made of materials such as  $\text{As}_2\text{Se}_3$  and Ge-As-Te-Se have been subjected to simulations for supercontinuum generation. These waveguides exhibit a wide bandwidth coverage, spanning from  $2$  to  $14\ \mu\text{m}$ <sup>[71,81]</sup>. However, achieving supercontinuum generation beyond  $5\ \mu\text{m}$  remains a material and fabrication challenge due to increased loss at longer wavelengths.<sup>[82]</sup>

### Frequency comb generation

Frequency combs, laser sources emitting light at a series of evenly spaced frequencies, were discovered in the late 1990s by John L. Hall and Theodor W. Hänsch. Their pioneering contributions to the field earned them the Nobel Prize in Physics in 2005. The comb-like spectra are achieved by generating a train of ultrashort laser pulses with a precisely controlled repetition rate. Frequency combs have numerous applications, including in GPS, satellite navigation, and space exploration.<sup>[83]</sup> Owing to their broadband nature, frequency combs in the LWIR spectrum hold great potential for spectroscopic studies of atoms



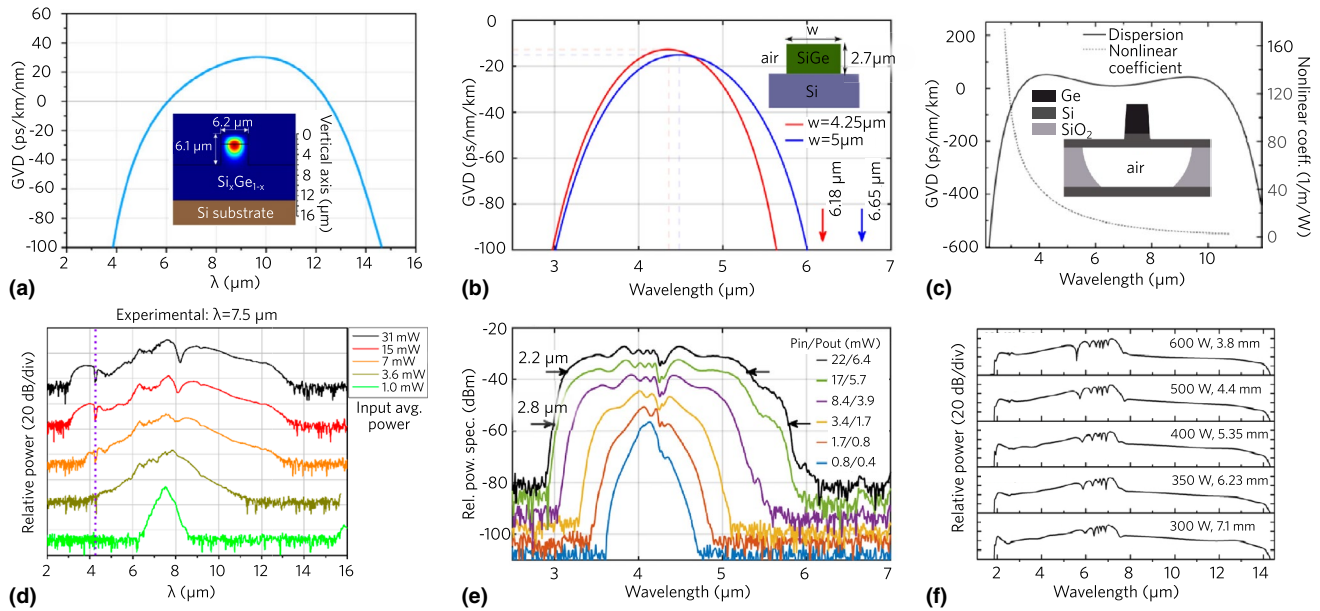


**Figure 4.** (a–c) Simulated dispersion of the waveguide geometries shown in the insets, for anomalous GVD,<sup>[64]</sup> all normal GVD<sup>[75]</sup> and low and flat GVD,<sup>[76]</sup> respectively. (d–f) The generated supercontinuum with geometries and dispersions shown from (a) to (c), respectively. Figures are adapted with permission from Refs. 64,75,76 © The Optical Society.

and molecules, with applications spanning chemistry, physics, and biology.<sup>[84,85]</sup>

To achieve broadband frequency comb generation in the LWIR, integrated low-loss passive microresonators such as Ge, diamond, and chalcogenide glass are promising candidates due to their wide transparency window. By carefully engineering the cavity dispersion, low-loss LWIR microresonators should be able to replicate the success of their near-infrared counterparts, such as Si<sub>3</sub>N<sub>4</sub> and Si platforms, in achieving a stable Kerr frequency comb.<sup>[4,86,87]</sup> Although chip-level LWIR frequency combs with flat gain curvature have been developed using powerful QCL with flexibility of dispersion engineering,<sup>[88,89]</sup> the bandwidth of QCL frequency combs is limited by the narrow gain profile preferred by low-threshold lasers,<sup>[90]</sup> making it challenging to achieve QCL frequency comb beyond 100 cm<sup>-1</sup> for broadband sensing applications. The threshold of the parametric oscillation, or sideband generation, can be expressed as follows<sup>[91–93]</sup>:

$$P_{th} = \frac{n\omega_0 A_{eff}}{8n_2 \eta f_{FSR} Q_T^2} \quad (3)$$

where  $n$  is refractive index,  $\omega_0$  is the optical frequency,  $A_{eff}$  is effective mode area,  $n_2$  is the Kerr coefficient,  $\eta = Q_T/Q_E$  is the waveguide-to-resonator loading factor,  $Q_T$  and  $Q_E$  are the total and external quality factors, and  $f_{FSR}$  is the FSR of the cavity. To generate a broadband microcomb in the LWIR, it is important to choose materials with low optical loss as the parametric threshold is inversely proportional to  $Q^2$ . Furthermore, using a micrometer-scale cavity with a larger free spectral range ( $f_{FSR}$ ) and relatively smaller effective area ( $A_{eff}$ ) can be beneficial. Ge WGM microresonators are a promising

candidate due to their record-high  $Q_{in} = 250,000$  at 8 μm. Ge has the largest refractive index ( $n$ ) and Kerr nonlinearity ( $n_2$ ) among all dielectric materials, making it a natural choice for broadband microcomb generation in the LWIR. The integrated dispersion parameter  $D_{int}$ , which describes the deviation of a given resonance from an equidistant frequency grid, can be calculated as  $D_{int} = \omega_n - \omega_0 - \mu \cdot D_1$ , where  $\omega_0$  is the angular frequency of the nearest mode close to the pump frequency  $\omega_{pmp}$ . Figure 5(a) shows the mode profile of the WGM located at the edge of the microresonator cavity, and Fig. 5(b) displays the calculated integrated dispersion  $D_{int}$  with a center frequency  $\omega_0$  of 28.2823 THz (10.6 μm in wavelength).

The dynamics of the Kerr frequency comb generation can be modeled using the generalized Lugiato-Lefever equation (LLE)<sup>[94,95]</sup>, which is derived from the nonlinear Schrödinger equation by only considering the third-order nonlinearity and in the reference frame moving with the group velocity:

$$\frac{\partial E(z, \tau)}{\partial z} = -\frac{\alpha}{2} E + i \sum \frac{\beta_k}{k!} \left( i \frac{\partial}{\partial \tau} \right)^k E + i \gamma |E|^2 E \quad (4)$$

where  $E(z, \tau)$  is the complex electric field propagating along  $z$  during the time  $\tau$ ,  $\alpha$  is the loss per unit length,  $\gamma = n_2 \omega_0 / (c_0 A_{eff})$  is the effective nonlinear coefficient,  $n_2$  is the Kerr nonlinear coefficient (i.e., the nonlinear refractive index),  $A_{eff}$  is the effective mode area in the resonator at the pump frequency,  $\beta_k$  is the  $k$ th-order Taylor expansion coefficient of the dispersion, and  $c_0$  is the speed of light in vacuum.

Figure 5(a) illustrates the integrated dispersion  $D_{int}$  of 100 μm diameter and 7 μm thickness WGM microresonators.

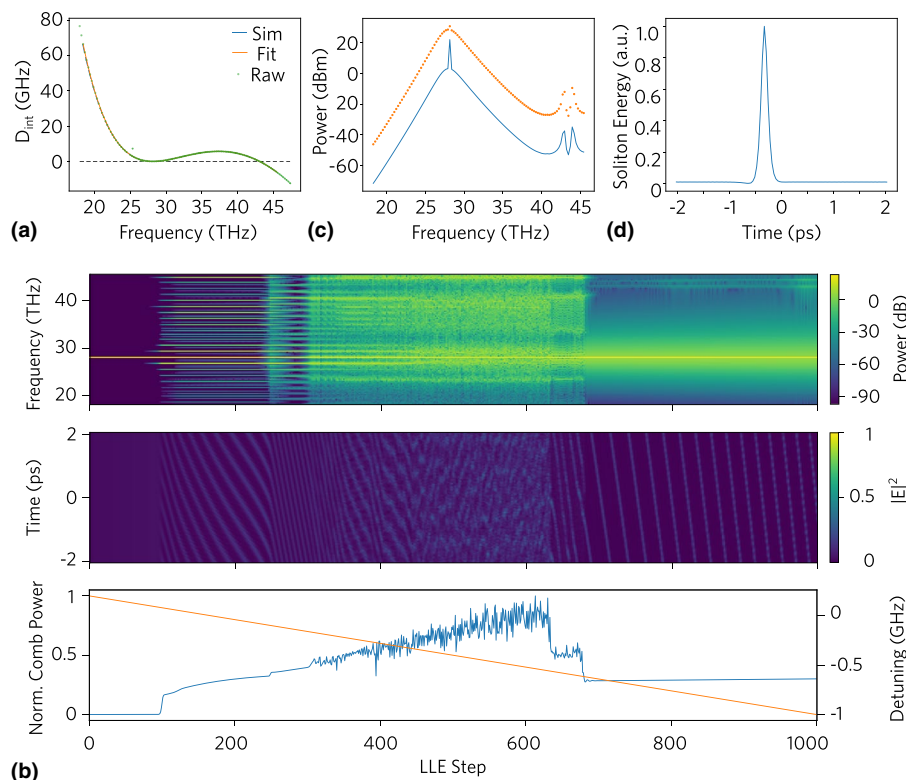


**Figure 5.** (a) Simulated integrated dispersion  $D_{int}$  of a WGM microresonator of 100  $\mu\text{m}$  in diameter and 7  $\mu\text{m}$  in thickness with  $\omega_0 = 28.15$  THz. Raw data points were generated from COMSOL eigenmode simulation. (b) Simulated dynamics of frequency comb generation by detuning from blue to red of 1.2 GHz with center pumping frequency of 28.15 THz using the dispersion parameter from (a). The three plots are: 2D plot of the comb power vs. frequency and LLE step (top), a 2D plot of the comb power vs. fast time and LLE step (middle), and a 1D plot of the comb power vs. LLE step with yellow line indicating of the detuning (bottom). Frequency spectrum (c) and temporal spectrum (d) are at  $-0.76$  GHz detuning, respectively.<sup>[95]</sup>

With  $\omega_0 = 28.15$  THz,  $A_{eff} = 15 \mu\text{m}^2$ ,  $n_2 = 2 \times 10^{-17} \text{m}^2/\text{W}$ , and a pump power of 200 mW, the frequency comb spectrum dynamics were generated in Fig. 5(b). The comb dynamics are represented by first blue-detuning the laser and then scanning across the resonance. To save computational resources, each simulation step contains multiple round trips that the pump laser underwent while the electric field has negligible changes. It is apparent from the frequency panel that the frequency comb formed as the laser scanned across the resonance. By further red-detuning the pump laser, the modes inside the microresonator cavity experienced clear chaos and reached a stable state at around  $-0.6$  GHz detuning in the time-domain panel in the middle. The existence of only one optical mode circulating inside the cavity indicates a single soliton state, which agrees well with a sharp power step in the comb power panel at the bottom. We plot the frequency spectrum and temporal spectrum at  $-0.76$  GHz detuning in Fig. 5(c) and (d), respectively. In the frequency spectrum, a clear broadband spectrum spanning from 20 to 45 THz can be observed, with a dispersive wave at 43 THz. Combining this with the single pulse of about 200 fs pulse width in the

temporal spectrum, we can confirm that a soliton state can be simulated inside the Ge microresonator.

### Fast detectors and modulators

As we have just discussed, the generation of broadband soliton microcombs requires high-quality factor microresonator with sufficient input power. The characterization of these microresonator frequency combs or the evaluation of the coherence among the comb lines is as much challenging as achieving the frequency comb itself, which usually requires fast detectors that allow I/Q demodulation at the repetition rate of the frequency comb.<sup>[96,97]</sup> III-V quantum well infrared photodetectors (QWIP) based on fs-capable intersubband transitions hold great promise for ultra-high-speed operation up to several hundreds of GHz at room temperature.<sup>[98,99]</sup> Double-metal patch antenna array takes advantage of the resonator effect, which can provide sub-wavelength electric field confinement and act as antennas. The active material of the QWIP is composed of five GaAs/AlGaAs quantum wells  $\sim 350$  nm thick GaAs/ $\text{Al}_{0.2}\text{Ga}_{0.8}\text{As}$  multi-quantum-well hetero-structure, absorbing at a wavelength of 8.9  $\mu\text{m}$  with a design according to an optimized

bound-to-continuum structure. This patch-array structure shows the substantially reduced dark current, which originates from the significantly enlarged ratio of the photonic collection area of each resonator over its electrical area.<sup>[98]</sup> By connecting the 2D array to the central electrode of a 50  $\Omega$  and tapering coplanar waveguide through an air bridge, the effect of parasitic capacitances brought by electrical connections and contact pads can be significantly reduced, which is the limiting factor of the RF operating frequency.<sup>[100]</sup> With individual resonators are connected by suspended gold wires, the QWIP detector has demonstrated heterodyne detection at  $\lambda \sim 10 \mu\text{m}$  with a nearly flat frequency response up to 70 GHz at room temperature, solely limited by the measurement system bandwidth. Notably, this detector has a good responsivity of 0.15 A/W at room temperature with an RC-limited 3 dB cutoff frequency  $>150$  GHz at 300 K, extracted with a small-signal equivalent circuit model.<sup>[99]</sup>

QWIP is a fast and sensitive technology for LWIR sensing. However, integrating it with photonic circuits, such as a waveguide, presents a challenge. To address this issue and develop compact and fieldable LWIR nonlinear photonic devices, integrating the photodetector on top of a waveguide is necessary for greater stability and reduced fabrication cost. Two-dimensional (2D) materials are a promising solution for on-chip photodetection, as they can be integrated with foreign materials without the restraint of lattice mismatch due to their layered lattice structures. Moreover, their bandgaps have a wide range from insulators, gapless semimetals to metallics, making them suitable for various applications.<sup>[101,102]</sup> For LWIR applications, gapless graphene is a material of great interest due to its high electron mobility for fast operation and broadband response from ultraviolet to terahertz. By integrating graphene with a Si waveguide, transferred and printed using microstructured polydimethylsiloxane (PDMS) stamp onto  $\text{CaF}_2$  substrates, the graphene photodetector operating at zero bias achieved a broadband responsivity of around 8 mA/W from 6.3 to 7.1  $\mu\text{m}$  in the LWIR with the help of waveguide integration and plasmonic enhancement.<sup>[103]</sup> The zero-bias operation for graphene-based integrated photodetectors offers great potential for fully integrated LWIR photonics with low power consumption, which is ideal for applications in wearable devices and smart sensors. Moreover, by integrating non-centrosymmetric metallic nanoantennas with graphene-based photodetectors, they exhibit zero-bias uncooled responsivity with three orders of magnitude higher than conventional bulk photovoltaic effect photodetectors. By observing the vectorial photoresponse, the polarization angle of incident light can be identified in a single device.<sup>[104]</sup>

Instead of relying on transfer-printing techniques to position the waveguide on a low-loss LWIR substrate with graphene as the photodetector,<sup>[103]</sup> an alternative method is to integrate the low-loss waveguide directly onto the substrate using traditional deposition techniques, leveraging the amorphous nature of chalcogenide glass.<sup>[105]</sup> By using a chalcogenide glass-on- $\text{CaF}_2$  PIC architecture with a split-gate photo thermoelectric graphene photodetector, integrated waveguide-photodetector devices can operate up to 5.2  $\mu\text{m}$ , with a Johnson noise-limited

noise-equivalent power of 1.1 nW/Hz<sup>1/2</sup>, no fall-off in photoreponse up to 1 MHz, and a predicted 3-dB bandwidth of  $f_{3\text{dB}} > 1$  GHz. The design and technology can also be applied in LWIR material platforms that we have discussed and proposed in this prospective, such as Ge and diamond, to enable operation in the longer wavelength range of the LWIR spectrum. This will be crucial for the development of compact, high-speed, and high-sensitivity distributed gas sensing and portable dual-comb spectroscopy systems.

As we briefly discussed earlier, high background noise due to thermal emission poses a challenge for LWIR photon detection. Therefore, on-chip waveguide modulators are crucial for high-precision photon detection in LWIR, especially when used in combination with lock-in amplifiers for synchronous detection. One such modulator is the Ge-on-Si carrier injection modulator, which forms a p-i-n structure on top of a Ge layer with heavily doped p-type and n-type regions implanted and separated by an intrinsic Ge waveguide with air cladding. Current versus modulation depth data for this modulator shows a 16.8 dB/A slope at 8  $\mu\text{m}$ , which is 5 times larger than that at 3.8  $\mu\text{m}$  when a linear curve is fit to both sets of data.<sup>[106]</sup> Another approach to achieve LWIR modulation is through graded SiGe waveguides on Si. By pumping the waveguide with NIR laser at 1.33  $\mu\text{m}$ , the excited free carriers inside the SiGe waveguide enhance LWIR absorption, reducing the output intensity of the LWIR signal.<sup>[107]</sup> This free-carrier-assisted modulation can work up to 11  $\mu\text{m}$ , much longer than the reported thermo-optic modulation which can only perform at 5  $\mu\text{m}$ . However, the latter is preferred in some applications, such as phase shifters, when the tuning range of the refractive index is large.<sup>[107,108]</sup>

## Prospective view

With the extensive exploration of low-loss materials for integrated LWIR nonlinear photonics and the development of new fabrication methods, we now see tremendous potential for achieving a fully integrated ultra-efficient photonic sensing system in the LWIR in a short time. However, directly duplicating the fabrication methods from NIR to LWIR may result in unavoidable material degradation, which must be adapted to the stringent requirements of LWIR. For example, the ion implantation damage in the smart-cut Si on insulator process should be carefully removed for mass production of Ge on insulator wafers.<sup>[109,110]</sup> After achieving low loss for both waveguides and suspended microresonators, the next challenge is to reach 0.5 dB/cm from racetrack microresonators. This will rely on the successful combination of multiple low-loss platforms, e.g., chalcogenide glass and single crystalline diamond can be used as the best bottom cladding substrate to hold the high-index intrinsic Ge.

The good news for LWIR is that we have both amorphous and crystalline low-loss materials, that can serve as different components in regard to different characteristics. For example, the chalcogenide glass can be sputtered to planarize the high-refractive index waveguide so that a solid-state laser can

be vertically coupled into.<sup>[111]</sup> If we look at fully integrated nonlinear photonic devices at the most developed NIR telecom band, we can easily figure out a minimum of three major low-loss components, substrate, waveguide and top cladding that is sufficient to enable full integration with solid-state lasers and detectors on a chip.<sup>[112,113]</sup> In principle, it is the right time to do so in the LWIR. Specifically, broadband Kerr frequency comb generated using a passive low-loss microresonator on-chip at LWIR has a unique position in connection from chip-scale device design and nonlinear photonics, because Q1 it can connect multi-watts QCL with the mode-locking for fs-scale ultrashort pulse generation, as we showed in the LLE simulation. This could provide an alternative solution at chip-level, in regards to the bulk and expensive OPA in the LWIR.

From an application perspective, chip-scale LWIR nonlinear photonic devices will enable high-resolution broadband dual-comb spectroscopy.<sup>[114,115]</sup> This will equip us with unprecedented miniaturized real-time broadband molecular sensing capacity. Combined with machine learning, it has much to offer for early disease detection at home and environment monitoring flying by drone. Considering the existing and well-developed chip-level QCL and QWIPs, the fast development of integrated nonlinear photonics in the LWIR will quickly make up the missing part for advanced sensing, imaging, and metrology.

## Acknowledgments

This work was sponsored by Research Council of Norway through the FRINATEK Program (Grant No. 302923). D.R. thanks the generous financial support from the FRIPRO Mobility Fellowship, Research Council of Norway. D.B. acknowledges support from AFOSR Grant No. FA9550-20-1-0192, NSF Grant ECCS-2046772, and ONR Grant N00014-21-1-2735; this research is funded in part by the Gordon and Betty Moore Foundation through Grant GBMF11446 to the University of Notre Dame to support the work of D.B.

## Funding

Open access funding provided by NTNU Norwegian University of Science and Technology (incl St. Olavs Hospital - Trondheim University Hospital).

## Declarations

### Conflict of interest

On behalf of all authors, the corresponding author states that there is no conflict of interest.

## Open Access

This article is licensed under a Creative Commons Attribution 4.0 International License, which permits use, sharing, adaptation, distribution and reproduction in any medium or format, as long as you give appropriate credit to the original author(s) and

the source, provide a link to the Creative Commons licence, and indicate if changes were made. The images or other third party material in this article are included in the article's Creative Commons licence, unless indicated otherwise in a credit line to the material. If material is not included in the article's Creative Commons licence and your intended use is not permitted by statutory regulation or exceeds the permitted use, you will need to obtain permission directly from the copyright holder. To view a copy of this licence, visit <http://creativecommons.org/licenses/by/4.0/>.

## References

1. J. Haas, B. Mizaiakoff, Advances in mid-infrared spectroscopy for chemical analysis. *Annu. Rev. Anal. Chem.* **9**, 45–68 (2016)
2. H. Kaplan, *Practical Applications of Infrared Thermal Sensing and Imaging Equipment*, vol. 75 (SPIE press, Bellingham 2007)
3. M. Vollmer, K.-P. Möllmann, *Infrared Thermal Imaging: Fundamentals, Research and Applications* (Wiley, Hoboken 2017)
4. S.A. Miller, M. Yu, X. Ji, A.G. Griffith, J. Cardenas, A.L. Gaeta, M. Lipson, Low-loss silicon platform for broadband mid-infrared photonics. *Optica* **4**(7), 707–712 (2017)
5. M.H. Pfeiffer, J. Liu, A.S. Raja, T. Morais, B. Ghadiani, T.J. Kippenberg, Ultrasmooth silicon nitride waveguides based on the Damascene reflow process: fabrication and loss origins. *Optica* **5**(7), 884–892 (2018)
6. B. Bendow, *Optical properties of highly transparent solids* (Springer Science & Business Media, Berlin 2012)
7. R.E. Hummel, *Electronic properties of materials*, vol. 3 (Springer, Berlin 2011)
8. C. Kittel, P. McEuen, *Introduction to solid state physics* (Wiley, Hoboken 2018)
9. F. Johnson, Lattice absorption bands in silicon. *Proc. Phys. Soc.* **73**(2), 265 (1959)
10. S. Fray, F. Johnson, J. Quarrington, N. Williams, Lattice bands in germanium. *Proc. Phys. Soc.* **85**(1), 153 (1965)
11. R. Collins, H. Fan, Infrared lattice absorption bands in germanium, silicon, and diamond. *Phys. Rev.* **93**(4), 674 (1954)
12. M.E. Thomas, W.J. Tropf, Optical properties of diamond. *Johns Hopkins APL Tech. Dig.* **14**(1), 16–23 (1993)
13. J.A. Savage, Optical properties of chalcogenide glasses. *J. Non-Cryst. Solids* **47**(1), 101–115 (1982)
14. N.K. Hon, R. Soref, B. Jalali, The third-order nonlinear optical coefficients of Si, Ge, and Si<sub>1-x</sub>Ge<sub>x</sub> in the midwave and longwave infrared. *J. Appl. Phys.* **110**(1), 9 (2011)
15. K. Bindra, H. Bookey, A. Kar, B. Wherrett, X. Liu, A. Jha, Nonlinear optical properties of chalcogenide glasses: Observation of multiphoton absorption. *Appl. Phys. Lett.* **79**(13), 1939–1941 (2001)
16. M. Levenson, N. Bloembergen, Dispersion of the nonlinear optical susceptibility tensor in centrosymmetric media. *Phys. Rev. B* **10**(10), 4447 (1974)
17. K. Zhang, G. Böhm, M.A. Belkin, Kerr nonlinearity and group velocity dispersion of InGaAs/InP and GaAsSb/InP waveguides in the mid-infrared. *APL Photonics* **8**(6), 066107 (2023)
18. J. Dismukes, L. Ekstrom, R. Paff, Lattice parameter and density in germanium-silicon alloys. *J. Phys. Chem.* **68**(10), 3021–3027 (1964)
19. D. Eaglesham, M. Cerullo, Low-temperature growth of Ge on Si(100). *Appl. Phys. Lett.* **58**(20), 2276–2278 (1991)
20. L. Colace, G. Masini, F. Galluzzi, G. Assanto, G. Capellini, L. Di Gaspare, E. Palange, F. Evangelisti, Metal. Ge-Si heterostructures for near-infrared light detection. *J. Vac. Sci. Technol. B: Microelectron. Nanometer Struct. Proc. Meas. Phenom.* **17**(2), 465–467 (1999)
21. M. Nedeljkovic, J.S. Penadés, C.J. Mitchell, A.Z. Khokhar, S. Stanković, T.D. Bucio, C.G. Littlejohns, F.Y. Gardes, G.Z. Mashanovich, Surface-grating-coupled low-loss Ge-on-Si rib waveguides and multimode interferometers. *IEEE Photonics Technol. Lett.* **27**(10), 1040–1043 (2015)



22. G.Z. Mashanovich, C.J. Mitchell, J.S. Penades, A.Z. Khokhar, C.G. Littlejohns, W. Cao, Z. Qu, S. Stanković, F.Y. Gardes, T.B. Masaud et al., Germanium midinfrared photonic devices. *J. Lightwave Technol.* **35**(4), 624–630 (2016)
23. M. Nedeljkovic, J.S. Penades, V. Mittal, G.S. Murugan, A.Z. Khokhar, C. Littlejohns, L.G. Carpenter, C.B. Gawith, J.S. Wilkinson, G.Z. Mashanovich, Germanium-on-silicon waveguides operating at mid-infrared wavelengths up to 8.5  $\mu$  m. *Opt. Express* **25**(22), 27431–27441 (2017)
24. K. Gallacher, R. Millar, U. Griškevičiūtė, L. Baldassarre, M. Sorel, M. Ortolani, D. Paul, Low loss Ge-on-Si waveguides operating in the 8–14  $\mu$  m atmospheric transmission window. *Opt. Express* **26**(20), 25667–25675 (2018)
25. M. Brun, P. Labeye, G. Grand, J.-M. Hartmann, F. Boulila, M. Carras, S. Nicoletti, Low loss SiGe graded index waveguides for mid-IR applications. *Opt. Express* **22**(1), 508–518 (2014)
26. M. Montesinos-Ballester, V. Vakarin, Q. Liu, X. Le Roux, J. Frigerio, A. Ballabio, A. Barzaghi, C. Alonso-Ramos, L. Vivien, G. Isella et al., Ge-rich graded SiGe waveguides and interferometers from 5 to 11  $\mu$  m wavelength range. *Opt. Express* **28**(9), 12771–12779 (2020)
27. B. Bendow, H.G. Lipson, S.P. Yukon, Multiphonon absorption in highly transparent semiconducting crystals. *Phys. Rev. B* **16**(6), 2684 (1977)
28. H.-Y. Liao, S. Jung, S. Chakravarty, R. T. Chen, M. A. Belkin: Low-Loss Ge-on- GaAs platform for mid-infrared photonics. 2017 Conference on Lasers and Electro- Optics (CLEO). IEEE. (2017), pp. 1–2
29. Y. Bai, M.T. Bulsara, E.A. Fitzgerald, Photoluminescence and secondary ion mass spectrometry investigation of unintentional doping in epitaxial germanium thin films grown on III-V compound by metal-organic chemical vapor deposition. *J. Appl. Phys.* **111**(1), 013502 (2012)
30. Y. Ruan, W. Li, R. Jarvis, N. Madsen, A. Rode, B. Luther-Davies, Fabrication and characterization of low loss rib chalcogenide waveguides made by dry etching. *Opt. Express* **12**(21), 5140–5145 (2004)
31. P.K. Mishra, V. Dave, J.N. Prasad, A.K. Choudhary, R. Chandra, Oblique angle sputtering of chalcogenide thin absorbing film. *Procedia Technol.* **14**, 219–227 (2014)
32. J. Hu, V. Tarasov, A. Agarwal, L. Kimerling, N. Carlie, L. Petit, K. Richardson, Fabrication and testing of planar chalcogenide waveguide integrated microfluidic sensor. *Opt. Express* **15**(5), 2307–2314 (2007)
33. X. Su, R. Wang, B. Luther-Davies, L. Wang, The dependence of photosensitivity on composition for thin films of Ge x As y Se 1-x-y chalcogenide glasses. *Appl. Phys. A* **113**, 575–581 (2013)
34. B. J. Eggleton, B. Luther-Davies, K. Richardson, Chalcogenide photonics. *Nat. Photonics* **5**(3), 141–148 (2011)
35. N. Hô, M.C. Phillips, H. Qiao, P.J. Allen, K. Krishnaswami, B.J. Riley, T.L. Myers, N.C. Anheier, Single-mode low-loss chalcogenide glass waveguides for the mid-infrared. *Opt. Lett.* **31**(12), 1860–1862 (2006)
36. B. Gholipour, M.J. Müller, Y. Li, S.S. Jo, Y. Cui, A. Mandal, B. Eggleton, M. Rochette, M. Rezaei, I. Alamgir et al., Roadmap on chalcogenide photonics. *J. Phys.: Photonics* **5**, 012501 (2022)
37. I. Aharonovich, J.C. Lee, A.P. Magyar, B.B. Buckley, C.G. Yale, D.D. Awschalom, E.L. Hu, Homoepitaxial growth of single crystal diamond membranes for quantum information processing. *Adv. Mater.* **24**(10), OP54–OP59 (2012)
38. Y.-J. Lee, A. Das, J.J. Talghader, High-Q diamond microresonators in the longwave infrared. *Opt. Express* **28**(4), 5448–5458 (2020)
39. M.M. Mirza, H. Zhou, P. Velha, X. Li, K.E. Docherty, A. Samarelli, G. Terner, D.J. Paul, Nanofabrication of high aspect ratio (50: 1) sub-10 nm silicon nanowires using inductively coupled plasma etching. *J. Vac. Sci. Technol. B, Nanotechnol. Microelectron.: Mater. Proc. Meas. Phenomena* **30**(6), 06FF02 (2012)
40. J. Hu, V. Tarasov, N. Carlie, N.-N. Feng, L. Petit, A. Agarwal, K. Richardson, L. Kimerling, Si-CMOS-compatible lift-off fabrication of low-loss planar chalcogenide waveguides. *Opt. Express* **15**(19), 11798–11807 (2007)
41. M.J. Burek, Y. Chu, M.S. Liddy, P. Patel, J. Rochman, S. Meesala, W. Hong, Q. Quan, M.D. Lukin, M. Lončar, High quality-factor optical nanocavities in bulk single-crystal diamond. *Nat. Commun.* **5**(1), 5718 (2014)
42. A. Faraon, P.E. Barclay, C. Santori, K.-M.C. Fu, R.G. Beausoleil, Resonant enhancement of the zero-phonon emission from a colour centre in a diamond cavity. *Nat. Photonics* **5**(5), 301–305 (2011)
43. B. Khanaliloo, M. Mitchell, A.C. Hryciw, P.E. Barclay, High-Q/V monolithic diamond microdisks fabricated with quasi-isotropic etching. *Nano Lett.* **15**(8), 5131–5136 (2015)
44. D. Ren, C. Dong, S.J. Addamane, D. Burghoff, High-quality microresonators in the longwave infrared based on native germanium. *Nat. Commun.* **13**(1), 5727 (2022)
45. N.C. MacDonald, SCREAM microelectromechanical systems. *Microelectron. Eng.* **32**(1–4), 49–73 (1996)
46. J.S. Penadés, A. Sánchez-Postigo, M. Nedeljkovic, A. Ortega-Moñux, J. Wangüemert- Pérez, Y. Xu, R. Halir, Z. Qu, A. Khokhar, A. Osman et al., Suspended silicon waveguides for long-wave infrared wavelengths. *Opt. Lett.* **43**(4), 795–798 (2018)
47. A. Osman, M. Nedeljkovic, J.S. Penades, Y. Wu, Z. Qu, A. Khokhar, K. Debnath, G. Mashanovich, Suspended low-loss germanium waveguides for the longwave infrared. *Opt. Lett.* **43**(24), 5997–6000 (2018)
48. K. Zhang, G. Böhm, M.A. Belkin, Mid-infrared microring resonators and optical waveguides on an InP platform. *Appl. Phys. Lett.* **120**(6), 061106 (2022)
49. H. Lin, L. Li, Y. Zou, S. Danto, J.D. Musgraves, K. Richardson, S. Kozacik, M. Murakowski, D. Prather, P.T. Lin et al., Demonstration of high-Q mid-infrared chalcogenide glass-on-silicon resonators. *Opt. Lett.* **38**(9), 1470–1472 (2013)
50. S. Suresh, S. Thomas, Comprehensive review of advances in the field of chalcogenide glass microresonators. *Int. J. Appl. Glass Sci.* **14**(2), 173–188 (2023)
51. D.A. Kozak, N.F. Tyndall, M.W. Pruessner, W.S. Rabinovich, T.H. Stievater, Germanium-on-silicon waveguides for long-wave integrated photonics: ring resonance and thermo-optics. *Opt. Express* **29**(10), 15443–15451 (2021)
52. J.M. Ramirez, Q. Liu, V. Vakarin, X. Le Roux, J. Frigerio, A. Ballabio, C. Alonso-Ramos, E.T. Simola, L. Vivien, G. Isella et al., Broadband integrated racetrack ring resonators for long-wave infrared photonics. *Opt. Lett.* **44**(2), 407–410 (2019)
53. H. Nguyen-Van, A.N. Baranov, Z. Loghmani, L. Cerutti, J.-B. Rodriguez, J. Tournet, G. Narcy, G. Boissier, G. Patriarche, M. Bahriz et al., Quantum cascade lasers grown on silicon. *Sci. Rep.* **8**(1), 7206 (2018)
54. S. Jung, D. Palaferri, K. Zhang, F. Xie, Y. Okuno, C. Pinzone, K. Lascola, M.A. Belkin, Homogeneous photonic integration of mid-infrared quantum cascade lasers with low-loss passive waveguides on an InP platform. *Optica* **6**(8), 1023–1030 (2019)
55. R. Wang, P. Täschler, Z. Wang, E. Gini, M. Beck, J. Faist, Monolithic integration of mid-infrared quantum cascade lasers and frequency combs with passive waveguides. *ACS Photonics* **9**(2), 426–431 (2022)
56. J. Faist, F. Capasso, D.L. Sivco, C. Sirtori, A.L. Hutchinson, A.Y. Cho, Quantum cascade laser. *Science* **264**(5158), 553–556 (1994)
57. B.G. Lee, M.A. Belkin, R. Audet, J. MacArthur, L. Diehl, C. Pflügl, F. Capasso, D.C. Oakley, D. Chapman, A. Napoleone et al., Widely tunable single-mode quantum cascade laser source for mid-infrared spectroscopy. *Appl. Phys. Lett.* **91**(23), 231101 (2007)
58. Y. Yao, A.J. Hoffman, C.F. Gmachl, Mid-infrared quantum cascade lasers. *Nat. Photonics* **6**(7), 432–439 (2012)
59. Y. Bai, N. Bandyopadhyay, S. Tsao, S. Slivken, M. Razeghi, Room temperature quantum cascade lasers with 27% wall plug efficiency. *Appl. Phys. Lett.* **98**(18), 181102 (2011)
60. Q. Lu, S. Slivken, D. Wu, M. Razeghi, High power continuous wave operation of single mode quantum cascade lasers up to 5 W spanning  $\lambda$  3.8–8.3  $\mu$  m. *Opt. Express* **28**(10), 15181–15188 (2020)
61. J. Faist, C. Gmachl, F. Capasso, C. Sirtori, D.L. Sivco, J.N. Baillargeon, A.Y. Cho, Distributed feedback quantum cascade lasers. *Appl. Phys. Lett.* **70**(20), 2670–2672 (1997)
62. R. Maulini, M. Beck, J. Faist, E. Gini, Broadband tuning of external cavity boundto- continuum quantum-cascade lasers. *Appl. Phys. Lett.* **84**(10), 1659–1661 (2004)
63. P. Del’Haye, O. Arcizet, M.L. Gorodetsky, R. Holzwarth, T.J. Kippenberg, Frequency comb assisted diode laser spectroscopy for measurement of microcavity dispersion. *Nat. Photonics* **3**(9), 529–533 (2009)
64. M. Montesinos-Ballester, C. Lafforgue, J. Frigerio, A. Ballabio, V. Vakarin, Q. Liu, J.M. Ramirez, X. Le Roux, D. Bouville, A. Barzaghi et al., On-chip

- mid-infrared supercontinuum generation from 3 to 13  $\mu$  m wavelength. *ACS Photonics* **7**(12), 3423–3429 (2020)
65. X. Liu, R.M. Osgood Jr., Y.A. Vlasov, W.M. Green, Mid-infrared optical parametric amplifier using silicon nanophotonic waveguides. *Nat. Photonics* **4**(8), 557–560 (2010)
  66. S. Slivken, M. Razeghi, High Power, Room Temperature InP-Based Quantum Cascade Laser Grown on Si. *IEEE J. Quantum Electron.* **58**(6), 1–6 (2022)
  67. S. Jung, J. Kirch, J.H. Kim, L.J. Mawst, D. Botez, M.A. Belkin, Quantum cascade lasers transfer-printed on silicon-on-sapphire. *Appl. Phys. Lett.* **111**, 211102 (2017)
  68. T. Komljenovic, L. Liang, R.-L. Chao, J. Hulme, S. Srinivasan, M. Davenport, J.E. Bowers, Widely-tunable ring-resonator semiconductor lasers. *Appl. Sci.* **7**(7), 732 (2017)
  69. P. Del'Haye, A. Schliesser, O. Arcizet, T. Wilken, R. Holzwarth, T.J. Kippenberg, Optical frequency comb generation from a monolithic microresonator. *Nature* **450**(7173), 1214–1217 (2007)
  70. T. Herr, K. Hartinger, J. Riemensberger, C. Wang, E. Gavartin, R. Holzwarth, M. Gorodetsky, T. Kippenberg, Universal formation dynamics and noise of Kerrfrequency combs in microresonators. *Nat. Photonics* **6**(7), 480–487 (2012)
  71. Z. Li, J. Yuan, C. Mei, F. Li, X. Zhou, B. Yan, Q. Wu, K. Wang, X. Sang, K. Long et al., Multi-octave mid-infrared supercontinuum and frequency comb generation in a suspended As<sub>2</sub>Se<sub>3</sub> ridge waveguide. *Appl. Opt.* **58**(31), 8404–8410 (2019)
  72. J.M. Dudley, G. Genty, S. Coen, Supercontinuum generation in photonic crystal fiber. *Rev. Mod. Phys.* **78**(4), 1135 (2006)
  73. C. Lafforgue, S. Guerber, J.M. Ramirez, G. Marcaud, C. Alonso-Ramos, X. Le Roux, D. Marris-Morini, E. Cassan, C. Baudot, F. Boeuf et al., Broadband supercontinuum generation in nitrogen-rich silicon nitride waveguides using a 300 mm industrial platform. *Photonics Res.* **8**(3), 352–358 (2020)
  74. M. Sinobad, C. Monat, B. Luther-Davies, P. Ma, S. Madden, D.J. Moss, A. Mitchell, D. Allieux, R. Orobtcchouk, S. Boutami et al., Mid-infrared octave spanning supercontinuum generation to 8.5  $\mu$  m in silicon-germanium waveguides. *Optica* **5**(4), 360–366 (2018)
  75. M. Sinobad, A. DellaTorre, R. Armand, B. Luther-Davies, P. Ma, S. Madden, A. Mitchell, D.J. Moss, J.-M. Hartmann, J.-M. Fedeli et al., Mid-infrared supercontinuum generation in silicon-germanium all-normal dispersion waveguides. *Opt. Lett.* **45**(18), 5008–5011 (2020)
  76. M. Yang, Y. Guo, J. Wang, Z. Han, K. Wada, L.C. Kimerling, A.M. Agarwal, J. Michel, G. Li, L. Zhang, Mid-IR supercontinuum generated in low-dispersion Ge-on-Si waveguides pumped by sub-ps pulses. *Opt. Express* **25**(14), 16116–16122 (2017)
  77. M.A. Ettabib, L. Xu, A. Bogris, A. Kapsalis, M. Belal, E. Lorent, P. Labeye, S. Nicoletti, K. Hammani, D. Syridis et al., Broadband telecom to mid-infrared supercontinuum generation in a dispersion-engineered silicon germanium waveguide. *Opt. Lett.* **40**(17), 4118–4121 (2015)
  78. G.P. Agrawal, *Nonlinear fiber optics. Nonlinear Science at the Dawn of the 21st Century* (Springer, Berlin 2000), p.195–211
  79. S. Dai, Y. Wang, X. Peng, P. Zhang, X. Wang, Y. Xu, A review of mid-infrared supercontinuum generation in chalcogenide glass fibers. *Appl. Sci.* **8**(5), 707 (2018)
  80. Y. Fang, C. Bao, S.-A. Li, Z. Wang, W. Geng, Y. Wang, X. Han, J. Jiang, W. Zhang, Z. Pan et al., Recent progress of supercontinuum generation in nanophotonic waveguides. *Laser Photonics Rev.* **17**, 2200205 (2023)
  81. D. Xia, Y. Huang, B. Zhang, Z. Yang, P. Zeng, H. Shang, H. Cheng, L. Liu, M. Zhang, Y. Zhu et al., On-chip broadband mid-infrared supercontinuum generation based on highly nonlinear chalcogenide glass waveguides. *Front. Phys.* **9**, 598091 (2021)
  82. Y. Yu, X. Gai, T. Wang, P. Ma, R. Wang, Z. Yang, D.-Y. Choi, S. Madden, B. Luther-Davies, Mid-infrared supercontinuum generation in chalcogenides. *Opt. Mater. Express* **3**(8), 1075–1086 (2013)
  83. T. Fortier, E. Baumann, 20 years of developments in optical frequency comb technology and applications. *Commun. Phys.* **2**(1), 153 (2019)
  84. N. Picqué, T.W. Hänsch, Frequency comb spectroscopy. *Nat. Photonics* **13**(3), 146–157 (2019)
  85. G. Villares, A. Hugi, S. Blaser, J. Faist, Dual-comb spectroscopy based on quantumcascade-laser frequency combs. *Nat. Commun.* **5**(1), 5192 (2014)
  86. J. Liu, G. Huang, R.N. Wang, J. He, A.S. Raja, T. Liu, N.J. Engelsen, T.J. Kippenberg, High-yield, wafer-scale fabrication of ultralow-loss, dispersion-engineered silicon nitride photonic circuits. *Nat. Commun.* **12**(1), 2236 (2021)
  87. A.L. Gaeta, M. Lipson, T.J. Kippenberg, Photonic-chip-based frequency combs. *Nat. Photonics* **13**(3), 158–169 (2019)
  88. A. Hugi, G. Villares, S. Blaser, H. Liu, J. Faist, Mid-infrared frequency comb based on a quantum cascade laser. *Nature* **492**(7428), 229–233 (2012)
  89. D. Burghoff, T.-Y. Kao, N. Han, C.W.I. Chan, X. Cai, Y. Yang, D.J. Hayton, J.-R. Gao, J.L. Reno, Q. Hu, Terahertz laser frequency combs. *Nat. Photonics* **8**(6), 462–467 (2014)
  90. L. Humbard, D. Burghoff, Analytical theory of frequency-modulated combs: generalized mean-field theory, complex cavities, and harmonic states. *Opt. Express* **30**(4), 5376–5401 (2022)
  91. T. Kippenberg, S. Spillane, K. Vahala, Kerr-nonlinearity optical parametric oscillation in an ultrahigh-Q toroid microcavity. *Phys. Rev. Lett.* **93**(8), 083904 (2004)
  92. X. Yi, Q.-F. Yang, K.Y. Yang, M.-G. Suh, K. Vahala, Soliton frequency comb at microwave rates in a high-Q silica microresonator. *Optica* **2**(12), 1078–1085 (2015)
  93. M.-G. Suh, C.Y. Wang, C. Johnson, K.J. Vahala, Directly pumped 10 GHz microcomb modules from low-power diode lasers. *Opt. Lett.* **44**(7), 1841–1843 (2019)
  94. L. Lugiato, F. Prati, M. Gorodetsky, T. Kippenberg, From the Lugiato-Lefever equation to microresonator-based soliton Kerr frequency combs. *Philos. Trans. R. Soc. A: Math. Phys. Eng. Sci.* **376**(2135), 20180113 (2018)
  95. G. Moille, Q. Li, X. Lu, K. Srinivasan, pyLLE: a fast and user friendly Lugiato-Lefever equation solver. *J. Res. Natl. Inst. Stand. Technol.* **124**, 1 (2019)
  96. D. Burghoff, Y. Yang, D.J. Hayton, J.-R. Gao, J.L. Reno, Q. Hu, Evaluating the coherence and time-domain profile of quantum cascade laser frequency combs. *Opt. Express* **23**(2), 1190–1202 (2015)
  97. Z. Han, D. Ren, D. Burghoff, Sensitivity of SWIFT spectroscopy. *Opt. Express* **28**(5), 6002–6017 (2020)
  98. D. Palaferri, Y. Todorov, A. Bigioli, A. Mottaghizadeh, D. Gacemi, A. Calabrese, A. Vasanelli, L. Li, A.G. Davies, E.H. Linfield et al., Room-temperature nine- $\mu$  m-wavelength photodetectors and GHz-frequency heterodyne receivers. *Nature* **556**(7699), 85–88 (2018)
  99. M. Haki, Q. Lin, S. Lepillet, M. Billet, J.-F. Lampin, S. Pirota, R. Colombelli, W. Wan, J. Cao, H. Li et al., Ultrafast quantum-well photodetectors operating at 10  $\mu$  m with a flat frequency response up to 70 GHz at room temperature. *ACS Photonics* **8**(2), 464–471 (2021)
  100. E.N. Grossman, J. Sauvageau, D.G. McDonald, Lithographic spiral antennas at short wavelengths. *Appl. Phys. Lett.* **59**(25), 3225–3227 (1991)
  101. G. Huang, Y. Hao, Y.D. Jia, J. Guo, H. Zhang et al., Recent progress in waveguide-integrated photodetectors based on 2D materials for infrared detection. *J. Phys. D: Appl. Phys.* **56**, 113001 (2023)
  102. F. Koppens, T. Mueller, P. Avouris, A. Ferrari, M. Vitiello, M. Polini, Photodetectors based on graphene, other two-dimensional materials and hybrid systems. *Nat. Nanotechnol.* **9**(10), 780–793 (2014)
  103. Y. Ma, Y. Chang, B. Dong, J. Wei, W. Liu, C. Lee, Heterogeneously integrated graphene/silicon/halide waveguide photodetectors toward chip-scale zero-bias longwave infrared spectroscopic sensing. *ACS Nano* **15**(6), 10084–10094 (2021)
  104. J. Wei, Y. Li, L. Wang, W. Liao, B. Dong, C. Xu, C. Zhu, K.-W. Ang, C.-W. Qiu, C. Lee, Zero-bias mid-infrared graphene photodetectors with bulk photoresponse and calibration-free polarization detection. *Nat. Commun.* **11**(1), 6404 (2020)
  105. J. Goldstein, H. Lin, S. Deckoff-Jones, M. Hempel, A.-Y. Lu, K.A. Richardson, T. Palacios, J. Kong, J. Hu, D. Englund, Waveguide-integrated mid-infrared photodetection using graphene on a scalable chalcogenide glass platform. *Nat. Commun.* **13**(1), 3915 (2022)
  106. T. Li, M. Nedeljkovic, N. Hattasan, W. Cao, Z. Qu, C.G. Littlejohns, J.S. Penades, L. Mastronardi, V. Mittal, D. Benedikovic et al., Ge-on-Si modulators operating at mid-infrared wavelengths up to 8  $\mu$  m. *Photonics Res.* **7**(8), 828–836 (2019)
  107. M. Montesinos-Ballester, V. Vakarín, J.M. Ramirez, Q. Liu, C. Alonso-Ramos, X. Le Roux, J. Frigerio, A. Ballabio, A. Barzaghi, L. Deniel et al., Optical

- modulation in Ge-rich SiGe waveguides in the mid-infrared wavelength range up to 11  $\mu$  m. *Commun. Mater.* **1**(1), 6 (2020)
108. A. Malik, S. Dwivedi, L. Van Landschoot, M. Muneeb, Y. Shimura, G. Lepage, J. Van Campenhout, W. Vanherle, T. Van Opstal, R. Loo et al., Ge-on-Si and Ge-on- SOI thermo-optic phase shifters for the mid-infrared. *Opt. Express* **22**(23), 28479–28488 (2014)
  109. C. Deguet, C. Morales, J. Dechamp, J. Hartmann, A. Charvet, H. Moriceau, F. Chieux, A. Beaumont, L. Clavelier, V. Loup, et al., Germanium-on-insulator (GeOI) structures realized by the Smart Cut/spl trade/technology. 2004 IEEE International SOI Conference (IEEE Cat. No. 04CH37573). IEEE, pp. 96-97 (2004)
  110. C.-M. Lim, Z. Zhao, K. Sumita, K. Toprasertpong, M. Takenaka, S. Takagi, Effects of hydrogen ion implantation dose on physical and electrical properties of Geon- insulator layers fabricated by the smart-cut process. *AIP Adv.* **10**(1), 015045 (2020)
  111. G. Roelkens, D. Van Thourhout, R. Baets, R. Nötzel, M. Smit, Laser emission and photodetection in an InP/InGaAsP layer integrated on and coupled to a Silicon-on- Insulator waveguide circuit. *Opt. Express* **14**(18), 8154–8159 (2006)
  112. B. Shen, L. Chang, J. Liu, H. Wang, Q.-F. Yang, C. Xiang, R.N. Wang, J. He, T. Liu, W. Xie et al., Integrated turnkey soliton microcombs. *Nature* **582**(7812), 365–369 (2020)
  113. C. Xiang, J. Liu, J. Guo, L. Chang, R.N. Wang, W. Weng, J. Peters, W. Xie, Z. Zhang, J. Riemensberger et al., Laser soliton microcombs heterogeneously integrated on silicon. *Science* **373**(6550), 99–103 (2021)
  114. Y. Yang, D. Burghoff, D.J. Hayton, J.-R. Gao, J.L. Reno, Q. Hu, Terahertz multiheterodyne spectroscopy using laser frequency combs. *Optica* **3**(5), 499–502 (2016)
  115. D.J. Benirschke, N. Han, D. Burghoff, Frequency comb ptychography. *Nat. Commun.* **12**(1), 4244 (2021)

**Publisher's Note** Springer Nature remains neutral with regard to jurisdictional claims in published maps and institutional affiliations.